Impact of Interfacial Disorder and Band Structure on the Resonant Conductance Oscillation in Quantum-Well-Based Magnetic Tunnel Junctions

Tianyi Ma, Bingshan Tao, Xavier Devaux, Hongxin Yang, Yalu Zuo, Sylvie Migot, Oleg Kurnosikov, Michel Vergnat, Xiufeng Han, Yuan Lu

Impact of Interfacial Disorder and Band Structure on the Resonant Conductance Oscillation in Quantum-Well-Based Magnetic Tunnel Junctions

Tianyi Ma, Bingshan Tao, Xavier Devaux, Hongxin Yang, Yalu Zuo, Sylvie Migot, Oleg Kurnosikov, Michel Vergnat, Xiufeng Han,* and Yuan Lu*

ABSTRACT:

Quantum well (QW) states formed in a double-barrier magnetic tunnel junction (DMTJ) enable the coherent resonant tunnelling of electrons. This phenomenon is significant for both the fundamental understanding of quantum transport and the development of advanced functionalities in spintronic devices. Careful engineering of the structural and chemical disorders at the QW/barrier interface is essential to maintain strong electron phase coherence, thereby ensuring reliable conductance oscillations in DMTJ. In this study, we systematically investigate the influence of interfacial disorders and band structure on QW-induced conductance oscillations in epitaxial Fe/MgAlOx/Fe (QW)/MgAlOx/Co/ Fe DMTJs grown by molecular beam epitaxy. It is found that the amplitude of QW oscillations is reduced to one-third due to chemical disorders caused by the incorporation of 2−4 monolayers of Co at the Fe (QW)/MgAlOx interface. In contrast, structural disorder induced by the incorporation of a single Fe monolayer completely suppresses the oscillations. In addition, the QW oscillation depends on the available majority Δ1 states of the injecting electrons at the Fermi level (EF) with k// = 0 from the upper electrode. Replacing the Fe upper electrode with Fe4N, which lacks a majority of Δ1 states at EF, significantly reduces the oscillation amplitude. Instead, using the bcc Co upper electrode, which possesses majority Δ1 states, results in no change in QW oscillation. Our findings highlight the critical role of interfacial disorder and band structure in QW-induced conductance oscillations, advancing the development of spin-dependent quantum resonant tunnelling applications.

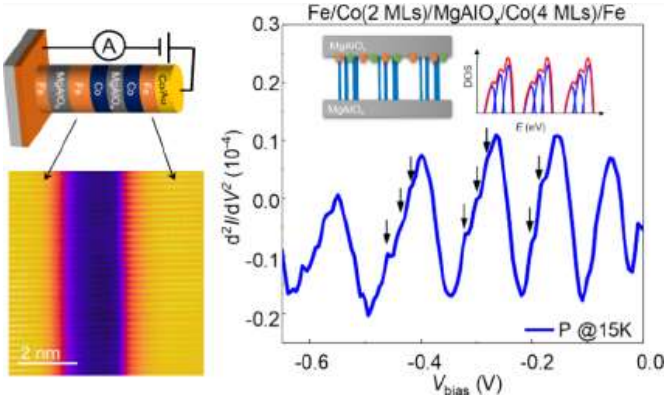

KEYWORDS: magnetic tunnel junction, quantum well, resonant tunnelling, magnetoresistance, electron phase coherence

INTRODUCTION

Double-barrier magnetic tunnel junctions (DMTJs) allow the formation of a quantum well (QW) in the metal layer between the two barriers, enabling resonant tunnelling of electrons when the energy of the injected electrons matches that of the discrete QW energy states. The DMTJ, with its high tunnelling magnetoresistance (TMR) and voltage-tunability, offers promising applications in next-generation magnetic random-access memory (MRAM),[1] magnetic sensors,[2] and spin logic devices.[3] Its ability to achieve TMR values from −4000 to +100% through voltage control[4] makes it especially suitable for devices requiring voltage-controllable and sign-reversible TMR effects. Previous studies have utilized both metallic layers (e.g., Cr) with symmetry-dependent band structures[2,5−10] and insulating barriers (e.g., Al2O3 or MgO) with higher barrier heights[4,11,12] to achieve QW resonant tunnelling. However, the thickness of the QW structure was limited to 1−2 nm to prevent electron dephasing within the QW. By replacing MgO with MgAlO*x* in the barrier, the lattice mismatch between the barrier and the Fe electrode can be minimized to less than 1%, resulting in better conservation of the electron phase. This leads to clear resonant QW oscillations even in a 12 nm thick metallic Fe layer at room temperature (RT).[13,14]In the Fe layer, the QW states are mainly formed by the majority Δ1 electron states. 50 14 When the Fermi level (*E*F) of the upper electrode matches the discrete QW states, resonant tunnelling of majority Δ1 electrons which possess the highest spin polarization occurs, significantly enhancing the TMR.[2] On the other hand, it has been reported that placing Co at the interface leads to a substantial increase in TMR, achieving up to 410% for epitaxial Co/MgO/Co MTJs[15] and 300% for FeCo*x*/MgO/FeCo*x* MTJs, both at RT.[16,17] The enhancement is explained by ab initio calculations showing that bcc Co only possesses majority-spin Δ1 states near the Fermi level,[18] significantly boosting the interface spin polarization. It would be intriguing to determine if placing Co at the interface could also enhance TMR in DMTJs. However, to observe QW resonant tunnelling, electron phase coherence must be maintained during reflection between the two potential barriers in the QW. Embedding Co could lead to decoherence due to the induced structural disorder and the interface roughness. Additionally, chemical disorder could provoke inelastic scattering within the QW and at the interface. These challenges could make achieving a high oscillation amplitude difficult. Therefore, further experiments are necessary to understand the effect of Co incorporation at the QW interfaces on TMR and QW oscillations. In this work, we systematically studied the impact of interfacial structural and chemical disorders, as well as the interface band structure, on the resonant oscillation in high-quality epitaxial Fe/MgAlO*x* DMTJs. Structural disorder was introduced by embedding Fe monolayers (MLs) at the interface or by varying the thickness of the bottom MgAlO*x* barrier. Chemical disorder was tuned by embedding Co MLs of different thicknesses (0−4 MLs) at the interface. We found that QW oscillations are more sensitive to structural disorder than to chemical disorder. Additionally, by comparing different upper electrodes (Fe, bcc Co and Fe4N), we discovered that the QW oscillation

amplitude also depends on the available majority-spin Δ1 electrons at *E*F with *k*// = 0. Understanding the critical role of structural and chemical disorders and the band structure of the upper electrode in QW oscillations will greatly promote the development of new spintronic devices operating in the quantum tunnelling regime.

RESULTS AND DISCUSSION

Sample Description and Growth Controlled by RHEED.

High-quality epitaxial magnetic tunnel junctions with a double-barrier structure were grown on single crystal MgO(001) substrates using molecular beam epitaxy (MBE) under a base pressure of 5 × 10−11 Torr. As depicted in Figure 1a, the QW forms within a metallic Fe layer sandwiched between two MgAlO*x* tunnelling barriers, with a detailed structure listed in Table 1.

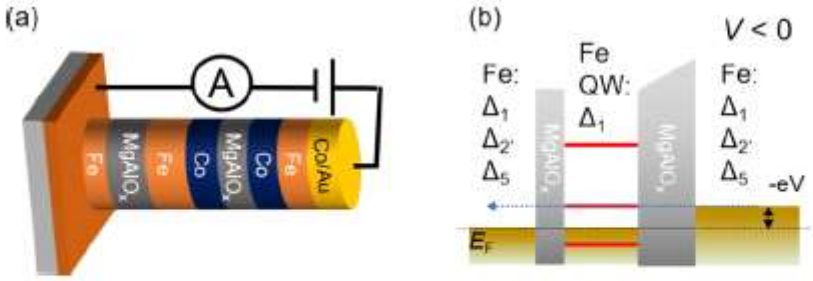

Figure 1. (a) Stack structure of DMTJ and setup of measurement. (b) Schematics of resonant tunneling in DMTJ show that only electrons with a majority of Δ_1 states are allowed to tunnel through the Fe QW.

The structure is intentionally designed with a thin barrier on the bottom and a thick barrier on the top because forming a QW on a thick barrier is challenging, as will be demonstrated and discussed below. Three sets of samples were grown to separately investigate the effects of band structure, interfacial chemistry, and structural disorder. To examine the influence of the upper electrode's band structure, Samples *A*, *B,* and *C* were grown with upper electrodes of Fe(10 nm), Co(4 MLs), and Fe4N(3 nm), respectively. To elucidate the effect of the top Co electrode, an additional control sample (Sample *K*) was grown. During the growth of the top Co(4 MLs) layer, a shutter was used to cover half of the substrate, allowing fabrication of two types of MTJs under exactly the same conditions for the bottom structures. For studying the effect of chemical disorder, different thicknesses of Co were embedded at the Fe/MgAlO*x* interface within the QW (2 MLs for Sample *D* and 4 MLs for Sample *E*). The third set of samples focused on studying the structural disorder originating from the interface roughness. To modify the roughness at the top QW interface, 1−2 MLs of Fe were deposited onto the annealed 10 nm Fe QW surface (Samples *F* and *G*). To adjust the roughness at the bottom QW interface, the bottom MgAlO*x* barrier was grown with varying thicknesses ranging from 5 to 10 MLs (Samples *H*, *I,* and *J*). The

epitaxial growth and annealing processes were controlled by reflection high-energy electron diffraction (RHEED).

Table 1. List of the Samples Studied in this Work

influence	sample no.	structure
band structure	sample *A* (ZZ825)	MgO(10 nm)/Fe(45 nm)/MgAlO$_x$(3 MLs)/Fe(10 nm)/MgAlO$_x$(12 MLs)/Fe(10 nm)/Co(20 nm)/Au(15 nm)
	sample *B* (ZZ818)	MgO(10 nm)/Fe(45 nm)/MgAlO$_x$(3 MLs)/Fe(10 nm)/MgAlO$_x$(12 MLs)/Co(4 MLs)/Fe(10 nm)/Co(20 nm)/Au(15 nm)
	sample *K* (ZZ841)	MgO(10 nm)/Fe(45 nm)/MgAlO$_x$(3 MLs)/Fe(10 nm)/MgAlO$_x$(12 MLs)/Co(4 MLs, half coved by shutter)/Fe(10 nm)/Co(20 nm)/Au(15 nm)
	sample *C* (ZZ2185)	MgO(10 nm)/Fe(45 nm)/MgAlO$_x$(3 MLs)/Fe(7 nm)/MgAlO$_x$(12 MLs)/Fe$_4$N(3 nm)/Co(20 nm)/Au(10 nm)
chemical disorder	sample *D* (ZZ816)	MgO(10 nm)/Fe(45 nm)/MgAlO$_x$(3 MLs)/Fe(10 nm)/Co(2 MLs)/MgAlO$_x$(12 MLs)/Co(4 MLs)/Fe(10 nm)/Co(20 nm)/Au(15 nm)
	sample *E* (ZZ744)	MgO(10 nm)/Fe(45 nm)/MgAlO$_x$(3 MLs)/Fe(10 nm)/Co(4 MLs)/MgAlO$_x$(12 MLs)/Co(4 MLs)/Fe(10 nm)/Co(20 nm)/Au(15 nm)
structural disorder	sample *F* (ZZ905)	MgO(10 nm)/Fe(45 nm)/MgAlO$_x$(3 MLs)/Fe(10 nm)/Fe(1 ML)/MgAlO$_x$(12 MLs)/Co(4 MLs)/Fe(10 nm)/Co(20 nm)/Au(15 nm)
	sample *G* (ZZ964)	MgO(10 nm)/Fe(45 nm)/MgAlO$_x$(3 MLs)/Fe(10 nm)/Fe(2 MLs)/MgAlO$_x$(12 MLs)/Co(4 MLs)/Fe(10 nm)/Co(20 nm)/Au(15 nm)
	sample *H* (ZZ874)	MgO(10 nm)/Fe(45 nm)/MgAlO$_x$(5 MLs)/Fe(10 nm)/MgAlO$_x$(12 MLs)/Fe(10 nm)/Co(20 nm)/Au (15 nm)
	sample *I* (ZZ879)	MgO(10 nm)/Fe(45 nm)/MgAlO$_x$(8 MLs)/Fe(10 nm)/MgAlO$_x$(12 MLs)/Fe(10 nm)/Co(20 nm)/Au(15 nm)
	sample *J* (ZZ894)	MgO(10 nm)/Fe(45 nm)/MgAlO$_x$(10 MLs)/Fe(10 nm)/MgAlO$_x$(12 MLs)/Fe(10 nm)/Co(20 nm)/Au(15 nm)

Detailed growth conditions can be found in the Methods section. Figure 2 shows the RHEED patterns and intensity oscillations obtained for Sample *E* during growth of the Co(4 MLs)/MgAlO*x*(12 MLs)/Co(4 MLs) structure. Clear oscillations can be observed during the growth of the first Co inserted layer (Figure 2a) and the MgAlO*x* barrier (Figure 2d), indicating a desired two-dimensional (2D) layer-by-layer epitaxial growth mode. The bright streaks and Kikuchi lines observed in the RHEED patterns of the bottom Co (Figure 2b,c) and the MgAlO*x* barrier (Figure 2e,f) further 133

confirm the good epitaxial growth. In contrast, the upper Co layer grown on the MgAlO*x* does not follow the layer-by-layer mode due to the poor wetting properties of metal on the oxide, as indicated by the absence of RHEED intensity oscillations in Figure 2g. The spotty pattern observed in Figure 2h,i indicates that the growth of Co on MgAlO*x* follows a three-dimensional (3D) growth mode, resulting in a rough Co surface. After the deposition of Fe on top of this surface and subsequent in situ 141

annealing, the surface becomes smooth again (see SI Note 1). For Sample *C*, the growth of Fe4N was performed by the evaporation of Fe in the presence of atomic and ionic nitrogen using an electron cyclotron resonance (ECR) plasma source. Detailed growth conditions can be found elsewhere.19

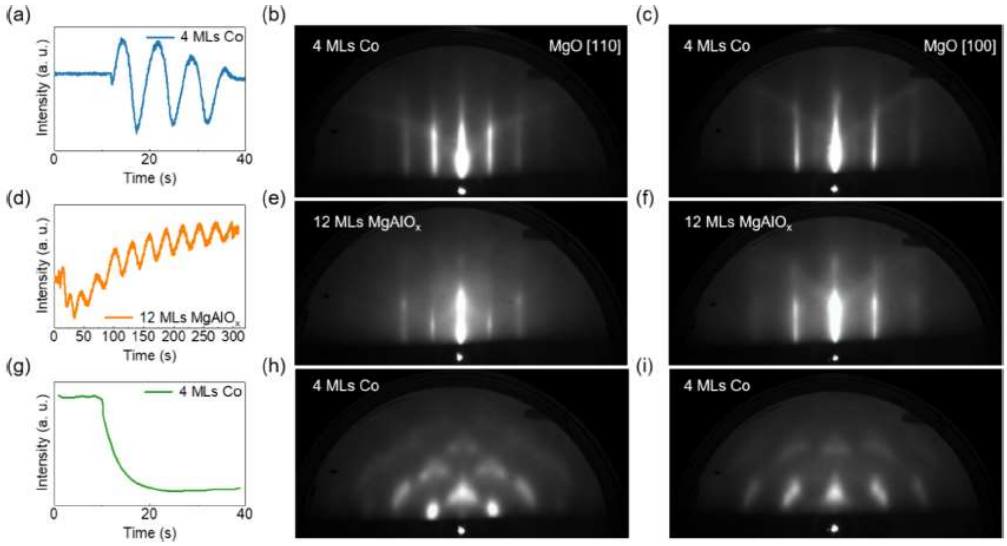

Figure 2. RHEED patterns of Sample *E* in different growth steps. (a) RHEED intensity evolution during the growth of the bottom 4 ML Co. (b,c) RHEED patterns of 4 ML Co along [110] and [100] azimuths of the MgO substrate. (d) RHEED intensity evolution during the growth of 12 ML $MgAlO_x$. (e,f) RHEED patterns of 12 MLs $MgAlO_x$ along [110] and [100] azimuths of MgO substrate. (g) RHEED intensity evolution during the growth of the top 4 ML Co. (h,i) RHEED patterns of 4 ML Co along [110] and [100] azimuths of MgO substrate.

Structure and Chemistry Study by STEM Combined with EELS.

High-resolution scanning transmission electron microscopy (HR-STEM) characterization was performed to verify the structure of the DMTJs. Figure 3a shows the high angle annular dark-field (HAADF) images for Sample *E* at a low-magnification and a high-resolution (HR) scale for the two barriers. Due to the varying electron scattering rates, raw HAADF images exhibit high contrast. Artificial colorization was applied to enhance the readability of the HR images and to make atomic columns visible in all phases. Sharp interfaces between the Co (in grey and orange) and MgAlO*x* (in dark grey and blue or red) can be observed. The two MgAlO*x* barriers are perfectly flat and continuous in the low-magnification image, indicating high-quality stack structures. The HR images further demonstrate the epitaxial growth characteristics with well-aligned atomic arrays between the Fe, MgAlO*x*, and Co layers. No structural disorder is observed at the top and bottom QW/barrier interfaces with Co insertion, as shown in Figure 3a. To check the chemical disorder at the interface, element distribution analyses were performed using STEM combined with spatially resolved EELS characterizations. Figure 3b,c presents semiquantitative Co maps and the atomic composition profiles drawn from chemical maps for Samples *D* and *E* with different thicknesses of the bottom Co insertion layer.

found in SI Note 2. From the Co maps, it is evident that the bottom Co layer is well-confined in both samples, in contrast to the wider distribution in the top Co layer, which is attributed to the larger roughness of the top Co layer due to the 3D growth mode. The 4 MLs of bottom Co (Figure 3c) have almost the same thickness distribution as the 2 MLs of Co (Figure 3b), but with a higher Co composition. These features are more visible in the atomic composition profiles. While the insertion of the bottom Co layer does not introduce a structural disorder, it could result in partial formation of Co*x*Fe1−*x* alloy

at the interface due to the atomic interdiffusion during the subsequent annealing procedure, which may induce chemical disorder at the Fe/MgAlO*x* interface.

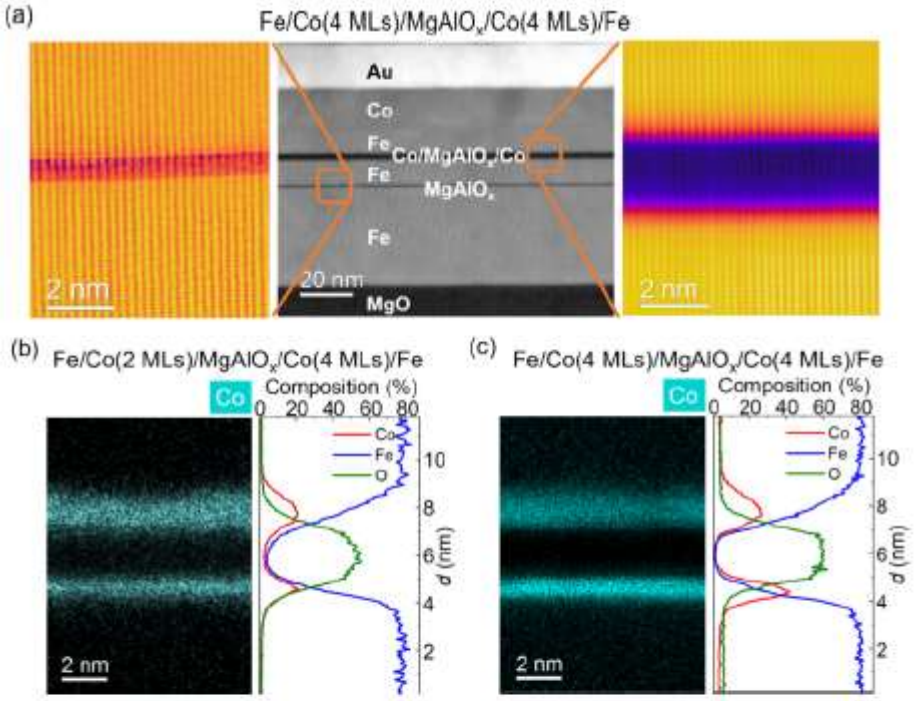

Figure 3. Interfacial structures and chemical maps of DMTJ stacks. (a) STEM-HAADF images of Sample *E* with different scales. Artificial colors are added to improve the readability. (b,c) Co maps and atomic composition profiles extracted from STEM-EELS for (b) Sample *D* and (c) Sample *E*.

Impact of the Band Structure on the QW Oscillation.

Magneto-transport measurements were conducted using a direct-current two-probe configuration, where a negative bias corresponds to electrons tunnelling from the top to the bottom electrode. Despite the presence of two MgAlO*x* insulating barriers in the stacks, the junction resistance is predominantly determined by the thicker barrier. The inset of Figure 4a shows the TMR curve of Sample *A* measured at 16 and 300 K for a bias voltage *V*bias = +10 mV. When the magnetizations of the middle Fe (free layer) and the top Fe (hard layer) are parallel 195

(antiparallel), the junction exhibits a low (high) resistance state. The TMR ratio is calculated by the definition TMR = (*R*AP − *R*P)/*R*P × 100%, where *R*P and *R*AP are the junction resistances in parallel (P) and antiparallel (AP) magnetic configurations, respectively. Figure 4a−c presents the bias dependence of the differential conductance (d*I*/d*V*) and Figure 4d,e displays the secondary differential conductance (d2*I*/d*V*2) for samples *A*−*C* with different top electrodes. All d*I*/d*V* curves have been normalized by their corresponding conductance in the P state at zero bias and 16 K (*G*P (0 V, 16 K)). During the *I*−*V*

measurements in the P state, we applied a 2 kOe in-plane magnetic field to saturate all Fe (Co) magnetization in the parallel direction. This ensures that the interface spins align with the bulk magnetization, effectively ruling out the influence of spin disorder on QW oscillations. The corresponding TMR curves are shown in the insets of Figure 4a–c, with the results summarized in Table 2. It is found that the insertion of the top 4 ML Co results in a reduction of TMR (16 K) from 176% (Inset of Figure 4a) to 149% (Inset of Figure 4b). Samples *A* and *B* exhibit evident conductance oscillation at only negative bias, while no oscillation is observed at positive bias (Figure 4a,b).

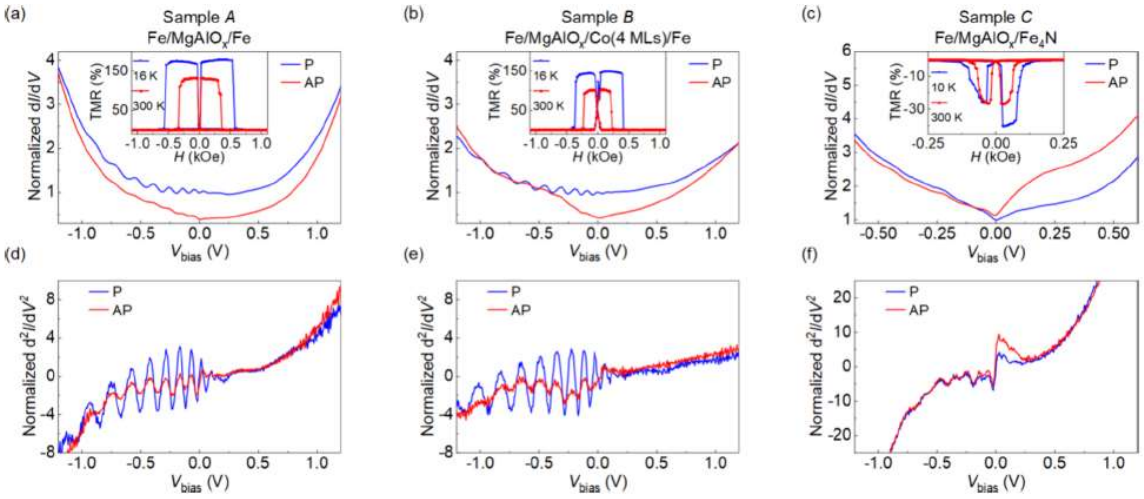

Figure 4. Bias dependence of differential conductance dI/dV and secondary differential conductance d^2I/dV^2 of samples with different top electrodes. (a–c) Bias dependence of normalized dI/dV (divided by G_P(0 V, 16 K)) at low temperature (LT) for (a) Sample *A*, (b) Sample *B*, and (c) Sample *C*. Insets in (a–c) show the TMR curves measured at LT and RT of corresponding samples. (d–f) Bias dependence of normalized d^2I/dV^2 at LT for (d) Sample *A*, (e) Sample *B*, and (f) Sample *C*.

In fact, this asymmetric bias dependence of the oscillations arises from the asymmetric stack structure. As shown in Figure 1b, the resistance and voltage drop across the thicker barrier were dominant. Under negative bias, the Fermi level of the top electrode is elevated, allowing the QW states to be probed, resulting in observable conductance oscillations. In contrast, under positive bias, the Fermi level of the bottom electrode remains pinned to the Fermi energy inside the QW, preventing the observation of QW oscillations. Comparing Figure 4d,e, it seems that the top insertion of Co (4 MLs) has a minimal impact on the oscillation amplitude. To avoid any different growth conditions for the Fe QW and MgAlO*x* barriers in Samples *A* and *B* for the comparison, we also examined a control sample (Sample *K*), in which half of the substrate was screened by a shutter during the growth of the top 4 MLs of the Co layer (see SI Note 3). Although the TMR ratio of Sample *K* is smaller than that of Samples *A* and *B*, the trend is the same, showing that the junction with 4 MLs Co insertion (49.9% at 17 K) is smaller than that without Co insertion (61% at 17 K). A detailed analysis of the conductance (d*I*/d*V*) (with data before normalization) reveals that the primary reason for the TMR decrease is the reduction in P

conductance while AP conductance remains almost unchanged. This could be due to the removal of the majority of Δ2' and Δ5 symmetries from the P conductance channel, as revealed by the bcc Co band structure (see SI Note 4). However, the conductance oscillation period and amplitude in both junctions, with and without the top Co layer, are exactly the same. These results confirm that the embedding of Co outside of QW has no effect on QW oscillations. Although the majority Δ1 density of states (DOS) in bcc Co is reduced compared to the Fe electrode (see SI Note 4),[16] the oscillation amplitude is still determined by the sharpness of the Fe QW states. For Sample *C*, where the top Fe electrode is replaced with an Fe4N electrode, we have observed a large negative TMR up to −41% at 10 K with *V*bias = + 0.45 V (Figure 4c). As shown in SI Note 4, the minority Δ1 and Δ5 bands of Fe4N cross the Fermi level, while no majority bands of Fe4N cross *E*F along the transport direction (*k*// = 0).[20] The negative TMR is mainly due to the strong Fe4N minority Δ1 DOS around +0.45V, which enhances the AP tunnelling conductance.[19] The QW oscillations are significantly attenuated, and the amplitudes for P and AP states are almost equal (Figure 4f). Since Fe QW states are formed by Fe majority Δ1 states, the lack of majority Δ1 states can explain the attenuation of the oscillation amplitude in the P state. However, in the AP state, a higher oscillation amplitude would be expected due to the minority Δ1 states at *E*F in the Fe4N band. Indeed, for strong QW oscillations to occur, the tunnelling electrons must not only meet the symmetry and spin conditions to match the QW states but also satisfy the *k*//=0 condition. Since the QW is formed between two barriers perfectly parallel to the sample plane, only electrons having *k*//=0 can maintain coherent phase when reflecting between the two potential barriers. Given the large lattice mismatch of 6.5% between Fe4N (3.795 A) and MgAl2O4 (4.212 A),[21] the Fe4N layer still contains many defects even though it is epitaxially grown on MgAlO*x*, as
275 revealed by STEM and RHEED characterizations (see SI Note 5). Therefore, the small oscillation in the AP state suggests that the electrons injected into the QW likely have a broad distribution of *k*//. Further optimization of Fe4N growth conditions could achieve a higher AP oscillation amplitude.

Table 2. Summary of Experimental Results for Samples with Different Co(Fe) Insertions

sample	bottom insertion (MLs)	top insertion (MLs)	oscillation amplitude in P state (a. u.)	oscillation amplitude in AP state (a. u.)	LT TMR (+10 mV)	RT TMR (+10 mV)
A			6.49	2.34	176%	133%
B		Co 4	6.99	2.49	149%	103%
C		Fe_4N (bulk)	3.28	3.86	−41% (+450 mV)	−27% (+450 mV)
D	Co 2	Co 4	2.13	0.97	110%	81%
E	Co 4	Co 4	2.35	0.55	66%	40%
F	Fe 1	Co 4			53%	33%
G	Fe 2	Co 4			32%	21%

Impact of Chemical Disorders on the QW Oscillation.

For the second set of samples, the upper Co embedding (4 MLs) remains unchanged, while we focus on the influence of the bottom Co embedding in QW on the oscillation amplitude. As revealed by the STEM-EELS analysis (Figure 3), the bottom Co insertion does not introduce structural disorder but only chemical disorder. As shown in Figure 5a,b, the TMR decreases for Samples *D* and *E* compared to Sample *B* without bottom Co insertion. This decrease is mainly due to the rise of *G*AP with the increase in thickness of the embedded Co layer. For Sample *E*, the AP conductance even exceeds the P conductance when *V*bias is higher than −0.37 V. The large increase of *G*AP could be attributed to the minority Δ1 DOS moving closer to the *E*F with higher Co concentration (see SI Note 4) or to the minority interface states at Co*x*Fe1−*x*/ MgAlO*x* interface.[16] As illustrated in Figure 5d,e, the bottom Co insertion in Samples *D* and *E* leads to a significant reduction in oscillation amplitude, down to one-third in both the P and AP states, while the thickness of the embedded layer is less relevant. Notably, a fine structure of the resonant oscillation in Sample *D* can be observed, as magnified in Figure 7d. The small step-like features in the oscillation are confirmed by repeated measurements (see SI Note 6). Both the decrease of oscillation amplitude and the small step-like features are due to the chemical disorder introduced by the Co insertion inside the QW, which negatively impacts the sharpness of the QW states. The impact of the chemical disorder will be discussed further along with first-principles calculations.

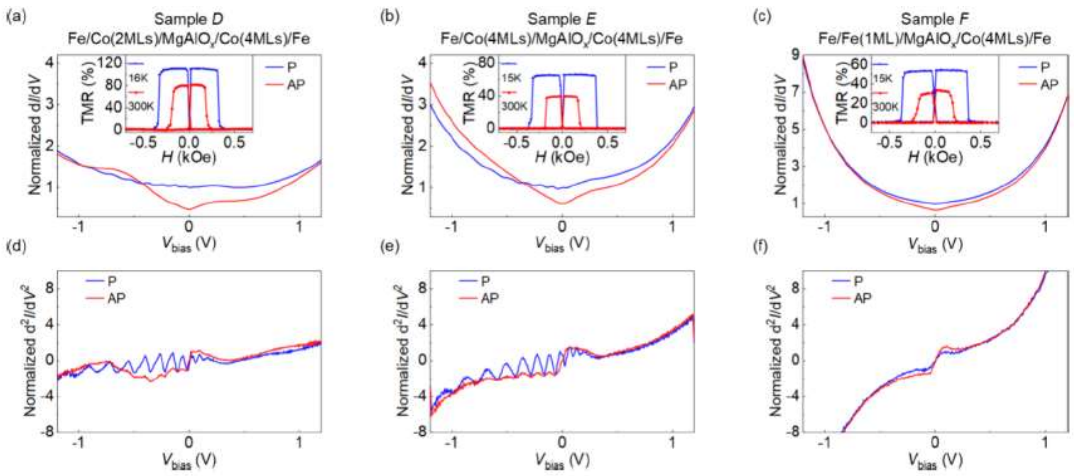

Figure 5. Bias dependence of differential conductance dI/dV and secondary differential conductance d^2I/dV^2 of samples with inner insertion of Co or Fe. (a–c) Bias dependence of normalized dI/dV (divided by G_P(0 V, 16 K)) at LT for (a) Sample *D*, (b) Sample *E*, and (c) Sample *F*. Insets in (a–c) show the TMR curves measured at LT and RT of corresponding samples. (d–f) Bias dependence of normalized d^2I/dV^2 at LT of (d) Sample *D*, (e) Sample *E*, and (f) Sample *F*.

Impact of Structural Disorders on the QW Oscillation. Two types of samples were used to study the effect of the interfacial structure disorder. To modify the top interface roughness, we deposited 1–2 MLs of Fe on the annealed 10 nm thick Fe surface, which exhibited a homoepitaxial growth mode (SI Note 7). Surprisingly, both Samples *F* (Figure 5c,f) and *G* (Figure S12) no longer show any conductance oscillation, indicating that the structural disorder introduced by monatomic roughness is detrimental to electron phase coherence and can completely eliminate the QW oscillations. Notably, for Samples

D and *E*, with Co presence in the QW, the post annealing temperature after the growth of the top Fe layer is 250 °C, which is sufficient to smooth the inner embedded Co layer and result in a high-quality Co/MgAlO*x* interface (Figure 3a).[15] In comparison, Sample *F* underwent a 400 °C post annealing, which is high enough to obtain a smooth Fe surface.[14,22] However, the quality of the Fe/ MgAlO*x* interface still does not meet the condition required for electron phase conservation to ensure good coherence. Therefore, the QW oscillation is more sensitive to interfacial structure disorder than the chemical disorder. Additionally, the TMR ratio of Samples *F* and *G* with Fe incorporation is even lower than that of Samples *D*, *E* with Co incorporation. Duluard et al. have reported an enhancement of TMR by monatomic roughness induced by incorporating a 0.5 ML Fe layer at the interface of Fe(001)/MgO/Fe MTJ.[23] The enhancement is explained by the reduced contribution of the
336 interfacial resonance states (IRS) to the junction conductance.[24] However, in our QW MTJ based on MgAlO*x* barrier, the IRS at Fe/MgAlO*x* interface could be significantlyreduced,[25] as no peak related to IRS is observed in the d2*I*/d*V*2 curve for the AP state[24] (Figure 5f). Therefore, interface roughness only negatively affects the TMR, leading to its deterioration. To study the effect of structural disorder at the bottom QW interface, three samples (Samples *H, I,* and *J*) with varying thicknesses for the bottom MgAlO*x* barrier were prepared. Figure 6 compares the d2*I*/d*V*2 curves at 16 K, revealing that the oscillations in d2*I*/d*V*2 at negative bias significantly decrease as the thickness of the bottom barrier increases. In addition, the TMR ratio also decreases with the increasing bottom barrier thickness (inset of Figure 6). This indicates that the bottom barrier thickness plays a crucial role in the quality of QW states. In fact, the lattice mismatch between MgO and Fe is approximately 4%,26 while the mismatch between MgAl2O4 and Fe is around 0.7−1%.27 As shown in Figure S5 (see SI Note 2), the composition of our MgAlO*x* barrier is approximately Mg:Al:O = 1:1.2:4.5, which is still quite different from the stoichiometric ratio of Mg:Al:O = 1:2:4. Consequently, the mismatch in our MgAlO*x* layer may exceed 1%. A thicker barrier can accumulate misfit strain from the underlying Fe layer, leading to increased surface roughness due to the formation of dislocations. This explains why the thicker bottom barrier leads to lower oscillation amplitude due to a broad distribution of the electron phase (dephasing) at the interface. Consequently, the QW oscillation amplitude is significantly reduced. Since the QW states are formed by the confined electron wave function reflecting between the two interfaces, the conservation of the electron phase implies that both interfaces play equally important roles. Therefore, even though the structure disorder at the top and bottom QW/barrier interfaces could be different, the behaviour of the diminishing QW oscillations should be similar. This contrasts with the TMR effect, where the bias dependence can reveal asymmetries between the barrier/top electrode and barrier/ bottom electrode interfaces.

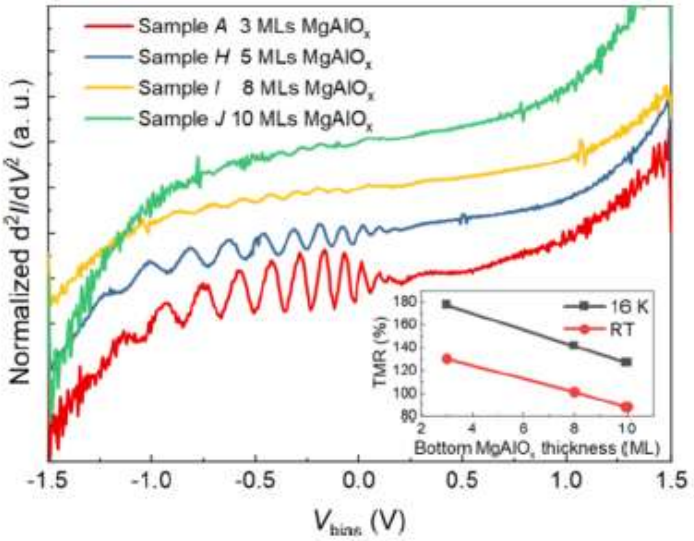

Figure 6. Normalized d^2I/dV^2 for DMTJs with different thicknesses of the bottom barrier (3 ML, 5 ML, 8 ML, and 10 ML). Inset: TMR ratio as a function of thickness of the bottom $MgAlO_x$ at 16 K and RT.

DISCUSSION

The QW states deduced from experimental results can be qualitatively compared with those calculated using a simple phase accumulation model (PAM).[28] The PAM considers the quantization condition for QW states as

$$2k_{\perp}d - \Phi_1 - \Phi_2 - \Phi_{\text{inf}} = 2\pi n$$

where

$$k_{\perp} = \sqrt{2m^*(E - E_{\text{L}})}/\hbar$$

is the electron momentum wave vector in the film perpendicular to the interface, *d* is the QW width , and

$$\Phi_1 = \Phi_2 = 2\sin^{-1}\sqrt{(E - E_{\text{L}})/(E_{\text{U}} - E_{\text{L}})} - \pi$$

are the phase shifts at the two QW/barrier interfaces reflecting the electrons. Furthermore, *m** is the effective mass of the electrons in QW, while *E*L and *E*U are the energies of the lower and upper edges of the barrier band gap. Φinf is an important parameter taking into account the additional phase shift at interfaces due to structural or chemical disorders, impurities, strain inhomogeneity, and other factors. Since the collected current is integrated over the whole junction area, the phase shift induced by a homogeneous distribution of Φinf will only shift the energy of QW states, but remarkable QW oscillations should still be observed. In contrast, an inhomogeneous broad distribution of < Φinf> will lead to a decay in the oscillation amplitude accompanied by an energy peak shift. As shown in the ab initio calculations, the QWs with and without Co insertion have different energy positions, confirming the effect of Φinf. Chemical disorder at the interface induced by the formation Co*x*Fe1−*x* alloy could

be responsible for the inhomogeneous spatial distribution of < Φinf>. Interestingly, Sample *D* with 2 MLs of Co insertion has an oscillation peak shape different from that of Sample *E* with 4 ML Co. In Figure 7d, the small stepped features (indicated by black arrows) suggest that several sets of QW states contribute to the integral tunnelling conductance. As schematically shown in Figure 7e, with a broad distribution of < Φinf> induced by chemical disorder at the interface, the QW energy peak positions also have a broad distribution within the same QW index over different spatial locations. Consequently, this smears the contrast of the current intensity as a function of bias and decreases the QW oscillation amplitude.

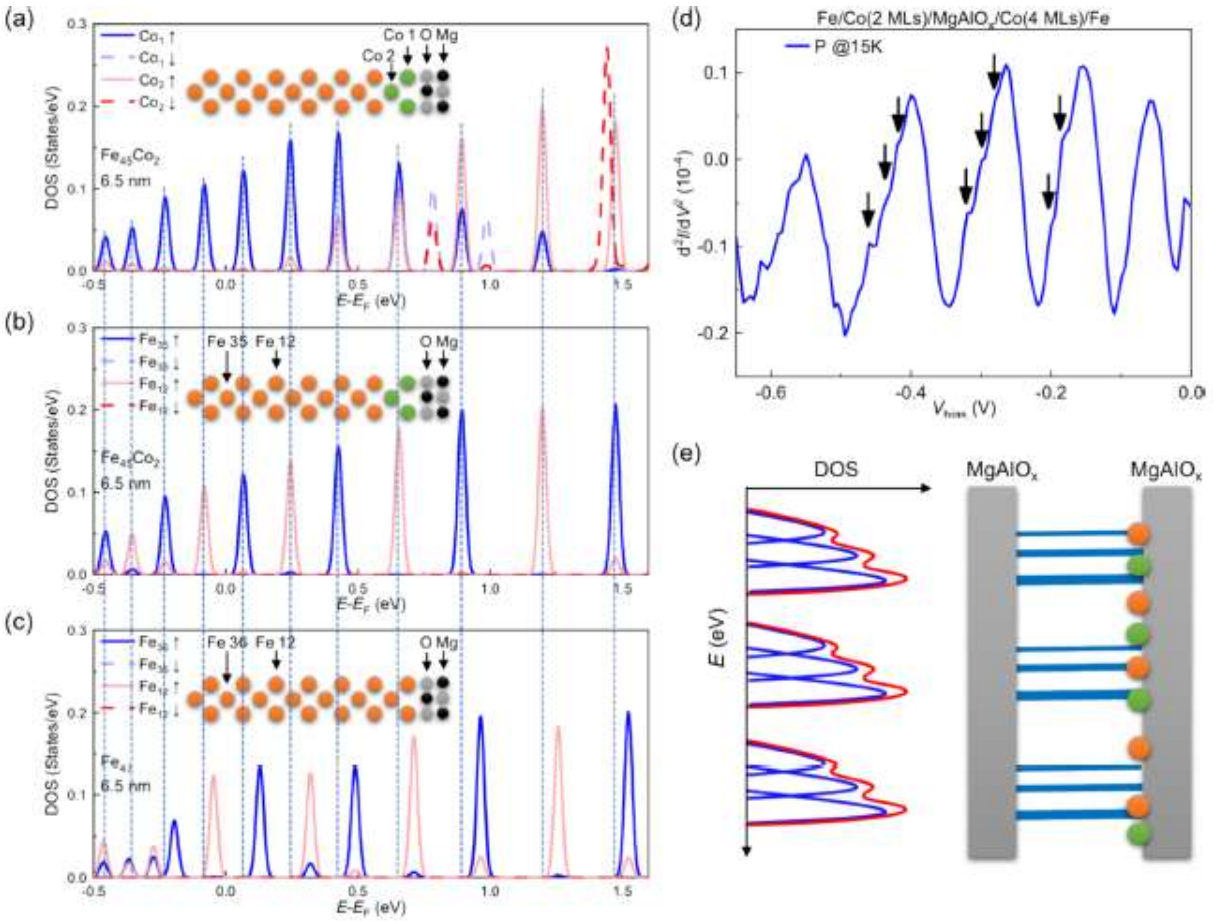

Figure 7. (a,b) QW states formed in *s*-resolved partial DOS at the Γ point for (a) interfacial Co and (b) central Fe in the QW of MgO(7 MLs)/Fe(45 MLs)/Co(2 MLs)/MgO(7 MLs). (c) *s*-resolved partial DOS at the Γ point for central Fe in the QW of MgO(7 MLs)/Fe(47 MLs)/MgO(7 MLs). In both cases, the total thickness of the QW layer is 47 MLs. Blue dashed lines are added to better visualize the shift of energy of QW states with Co insertion. (d) Experimentally measured fine structure in d^2I/dV^2 of Sample *D*. The substeps are marked by black arrows. (e) Schematics of the DOS distribution with three sets of QW states in QW MTJ with both Fe and Co at the QW/barrier interface.

Compared with chemical disorder, structural disorder at the interface not only introduces a broad distribution of < Φinf>, but also effectively modifies the QW width *d* which is more detrimental to phase coherence and resonant oscillations. The TMR in our QW MTJ with Co insertion is found to be much lower than that of the normal MgAlO*x* MTJ with Co insertion (284% at 14 K) (see SI Note 8). There are two possible reasons for this difference. First, for the QW MTJ, the upper electrode is annealed at 250 °C to minimize the chemical disorder in the QW, whereas for the normal MTJ, the post annealing was done at 400 °C. The different annealing temperatures can significantly influence the

TMR. Second, the band structure of QW is different from that of the normal MTJ. The Δ1 symmetry nature of QW states favours only Δ1 symmetry electrons with $k//$ = 0 for tunnelling through the QW resonances (Figure 1b), while the tunnelling in the normal MTJ also involves other $k// \neq 0$ and extra symmetry (Δ2', Δ5) channels.[8] In addition, the contribution of the CoFe/MgAlO*x* interface states[16,24] in normal MTJ could also play an important role in the symmetry-dependent tunnelling and therefore should affect the TMR.

CONCLUSIONS

In summary, we have conducted a comprehensive study of the effects of interfacial structure and chemical disorder as well as the interface band structure on the resonant QW-induced conductance oscillation in high-quality epitaxial Fe/MgAlO*x* DMTJs. We found that the QW oscillations are more sensitive to structural disorder than chemical disorder. Chemical disorder induced by Co insertion in the QW results in a broadening of the electron phase distribution and consequently reduces the conductance oscillation amplitude to one-third. However, atomic roughness after 1 ML Fe embedding completely suppresses all conductance oscillations. Furthermore, by comparing different top electrodes (Fe, bcc Co, and Fe4N), we established that the QW oscillation amplitude also depends on the availability of majority-spin Δ1 electrons at *E*F with $k//$ = 0 at the top electrode. Understanding the roles of structural and chemical disorders and the band structure in the QW oscillation is critical to design a high-performance device. With future efforts to reduce the junction size and QW thickness, as well as to optimize the composition of the MgAlO*x* barrier, we anticipate further improvements in the performance of QW MTJs, bringing them closer to practical spintronic quantum applications.

METHODS

Sample Preparation. All samples were fabricated in an MBE system on single crystal MgO (001) substrates. The growth process described below uses Sample *E* as an example. Initially, the substrate was annealed at 650 °C for 60 min, followed by the deposition of a 10 nm MgO seed layer. The first Fe layer was then deposited at RT via e-beam evaporation and subsequently annealed in situ at 500 °C for 30 min to smooth the surface. The first MgAlO*x* barrier was grown at approximately 80 °C with the growth process monitored by RHEED. two-dimensional layer-by-layer growth mode of MgAlO*x* was confirmed by the oscillation of the RHEED intensity. Next, the second Fe layer was deposited at about 70 °C and annealed in situ at 400 °C for 20 min, followed by the deposition of a 4 ML thick Co insertion layer and the second MgAlO*x* barrier at about 80 °C. Sequentially, another 4 ML thick Co layer was deposited on the MgAlO*x*, followed by a third deposition of a 10 nm thick Fe at about 70 °C and an annealing in situ at 250 °C for 30 min (except at 400 °C for Samples *A* and *F*). Finally, a 20 nm Co layer was deposited above the Fe layer to enhance the coercivity, and 15 nm Au was used to prevent the

oxidation. RHEED patterns obtained during the growth of the Sample *E* are shown in SI Note 1. Magneto-Transport Measurements. The multilayers were then patterned into junctions with areas ranging from 10 × 10 μm2 to 20 × 20 μm2 using standard ultraviolet lithography combined with Ar+ ion etching. Transport measurements were carried out in a cryostat cooled with liquid helium with electrical magnets. A Keithley 2450 instrument was used to apply the bias voltage to the DMTJ and measure the current. STEM-EELS Characterizations. HR-STEM combined with spatially resolved EELS was performed by using a JEOL ARM200F microscope (cold FEG) equipped with a GATAN GIF quantum energy filter. The microscope was operated at 200 kV. HAADF, annular dark-field (ADF), and bright-field (BF) images were simultaneously recorded for analysing the heterostructures, while only the HAADF signal was recorded during the EELS mapping. EELS spectrum images (SIs) were recorded with a probe current of about 50 pA. Two EELS-SIs were recorded simultaneously: one for the low-loss part containing the zero-loss and the other for the core loss, allowing advanced data postprocessing (energy drift correction, multiple scattering corrections). A multivariate statistical analysis software (temDM MSA) was used to improve the quality of the STEM-EELS data by denoising the core-loss SI before processing to draw quantitative chemical maps.[29] Thin lamellae were extracted by focused ion beam (FIB) milling using a FEI Helios Nanolab 600i dual beam. First-Principles Calculations. First-principles calculations were performed using the Vienna ab initio simulation package (VASP).[30−32] In all calculations, the exchange-correlation potentials were treated with the generalized gradient approximation (GGA) of the Perdew−Burke−Ernzerhof (PBE) function. The cut-off energy was 535
set to 420 eV. A Γ-centered 9 × 9 × 1 *k*-mesh was used in the structure relaxation, and the QW states were extracted at the Γ point. The convergence energy and force of the heterostructure were 10−7 eV and 0.001 eV/A, respectively. More details of the calculation can be found in our previous work.[14]

Accepted: August 19, 2024

Supporting Information

RHEED patterns of Sample E at different growth steps, STEM-EELS element maps of Samples *B*, *D,* and *E* with different Co insertion at Fe/MgAlO*x* interface inside QW, RHEED patterns and magneto-transport measurements of the control Sample *K*, symmetry-dependent band structure of bcc Fe, bcc Co, and Fe4N, STEM-HAADF images and RHEED pattern of Sample *C* with Fe4N top electrode, repetition measurements to confirm substep features in d*I*2/d*V*2 curves, RHEED patterns and intensity oscillation of Samples *F* and *G* with different Fe insertion at Fe/MgAlO*x* interface in the QW, and 555
RHEED and magneto-transport measurements on single barrier MgAlO*x* MTJ with Co insertion (PDF)

■AUTHOR INFORMATION

Corresponding Authors

Xiufeng Han − *Beijing National Laboratory for Condensed Matter Physics, Institute of Physics, University of Chinese Academy of Sciences, Chinese Academy of Sciences, Beijing 100190, China;* orcid.org/0000-0001-8053-793X; Email: xfhan@iphy.ac.cn

Yuan Lu − *CNRS-Université de Lorraine, UMR 7198, Institut Jean Lamour, 54011 Nancy, France;* orcid.org/0000-0003-3337-8205; Email: yuan.lu@univ-lorraine.fr

Authors

Tianyi Ma − *CNRS-Université de Lorraine, UMR 7198, Institut Jean Lamour, 54011 Nancy, France; Beijing National Laboratory for Condensed Matter Physics, Institute of Physics, University of Chinese Academy of Sciences, Chinese Academy of Sciences, Beijing 100190, China;* orcid.org/0000-0002-5987-6459

Bingshan Tao − *CNRS-Université de Lorraine, UMR 7198, Institut Jean Lamour, 54011 Nancy, France; Beijing National Laboratory for Condensed Matter Physics, Institute of Physics, University of Chinese Academy of Sciences, Chinese Academy of Sciences, Beijing 100190, China*

Xavier Devaux − *CNRS-Université de Lorraine, UMR 7198, Institut Jean Lamour, 54011 Nancy, France;* orcid.org/0000-0001-5694-464X

Hongxin Yang − *Center for Quantum Matter, School of Physics, Zhejiang University, Hangzhou 310058, China;* orcid.org/0000-0003-2627-0888

Yalu Zuo − *CNRS-Université de Lorraine, UMR 7198, Institut Jean Lamour, 54011 Nancy, France*

Sylvie Migot − *CNRS-Université de Lorraine, UMR 7198, Institut Jean Lamour, 54011 Nancy, France*

Oleg Kurnosikov − *CNRS-Université de Lorraine, UMR 7198, Institut Jean Lamour, 54011 Nancy, France*

Michel Vergnat − *CNRS-Université de Lorraine, UMR 7198, Institut Jean Lamour, 54011 Nancy, France*

ACKNOWLEDGMENTS

We acknowledge Caihua Wan for the discussion. This work is supported by the French National Research Agency (ANR) SOTspinLED project (No. ANR-22-CE24-0006-01). Experiments were conducted using equipment from the CC-Davm platform and the CC-3M platform, both funded by FEDER (EU), ANR, the Region Lorraine, and the metropole of Grand Nancy.

REFERENCES

(1) Scheike, T.; Wen, Z.; Sukegawa, H.; Mitani, S. Enhanced Tunnel Magnetoresistance in Fe/Mg4Al-O-x/Fe(001) Magnetic Tunnel Junctions. *Appl. Phys. Lett.* 2022, *120* (3), No. 032404.

(2) Xiang, Q.; Sukegawa, H.; Belmoubarik, M.; Al-Mahdawi, M.; Scheike, T.; Kasai, S.; Miura, Y.; Mitani, S. Realizing Room-Temperature Resonant Tunnel Magnetoresistance in Cr/Fe/MgAl2O4 Quasi-Quantum Well Structures. *Adv. Sci.* 2019, *6* (20), No. 1901438.

(3) Thomas, A.; Meyners, D.; Ebke, D.; Liu, N.-N.; Sacher, M. D.;Schmalhorst, J.; Reiss, G.; Ebert, H.; Huetten, A. Inverted Spin Polarization of Heusler Alloys for Spintronic Devices. *Appl. Phys. Lett.* 2006, *89* (1), No. 012502.

(4) Iovan, A.; Andersson, S.; Naidyuk, Y. G.; Vedyaev, A.; Dieny, B.; Korenivski, V. Spin Diode Based on Fe/MgO Double Tunnel Junction. *Nano Lett.* 2008, *8* (3), 805−809.

(5) Niizeki, T.; Tezuka, N.; Inomata, K. Enhanced Tunnel Magnetoresistance Due to Spin Dependent Quantum Well Resonance in Specific Symmetry States of an Ultrathin Ferromagnetic Electrode. *Phys. Rev. Lett.* 2008, *100* (4), No. 047207.

(6) Yuasa, S.; Nagahama, T.; Suzuki, Y. Spin-Polarized Resonant Tunneling in Magnetic Tunnel Junctions. *Science* 2002, *297* (5579), 234−237.

(7) Nagahama, T.; Yuasa, S.; Suzuki, Y.; Tamura, E. Quantum Size Effect in Magnetic Tunnel Junctions with Ultrathin Fe(001) Electrodes. *J. Appl. Phys.* 2002, *91* (10), 7035−7037.

(8) Greullet, F.; Tiusan, C.; Montaigne, F.; Hehn, M.; Halley, D.; Bengone, O.; Bowen, M.; Weber, W. Evidence of a Symmetry-Dependent Metallic Barrier in Fully Epitaxial MgO Based Magnetic Tunnel Junctions. *Phys. Rev. Lett.* 2007, *99* (18), No. 187202.

(9) Sheng, P.; Bonell, F.; Miwa, S.; Nakamura, T.; Shiota, Y.; Murakami, S.; Lam, D. D.; Yoshida, S.; Suzuki, Y. Detailed Analysis of Spin-Dependent Quantum Interference Effects in Magnetic Tunnel Junctions with Fe Quantum Wells. *Appl. Phys. Lett.* 2013, *102* (3), No. 032406.

(10) Teixeira, J. M.; Costa, J. D.; Ventura, J.; Sousa, J. B.; Wisniowski, P.; Freitas, P. P. Observation of Spin-Dependent Quantum Well Resonant Tunneling in Textured CoFeB Layers. *Appl. Phys. Lett.* 2014, *104* (11), No. 112414.

(11) Nozaki, T.; Tezuka, N.; Inomata, K. Quantum Oscillation of the Tunneling Conductance in Fully Epitaxial Double Barrier Magnetic Tunnel Junctions. *Phys. Rev. Lett.* 2006, *96* (2), No. 027208.

(12) Liu, R. S.; Yang, S.-H.; Jiang, X.; Zhang, X.-G.; Rettner, C.; Gao, L.; Topuria, T.; Rice, P. M.; Zhang, W.; Canali, C. M.; Parkin, S. S. P. CoFe Alloy as Middle Layer for Strong Spin Dependent Quantum Well Resonant Tunneling in MgO Double Barrier Magnetic Tunnel Junctions. *Phys. Rev. B* 2013, *87* (2), No. 024411.

(13) Tao, B.; Wan, C.; Tang, P.; Feng, J.; Wei, H.; Wang, X.; Andrieu, S.; Yang, H.; Chshiev, M.; Devaux, X.; Hauet, T.; Montaigne, F.; Mangin, S.; Hehn, M.; Lacour, D.; Han, X.; Lu, Y. Coherent Resonant Tunneling through Double Metallic Quantum Well States. *Nano Lett.* 2019, *19* (5), 3019−3026.

(14) Tao, B. S.; Yang, H. X.; Zuo, Y. L.; Devaux, X.; Lengaigne, G.; Hehn, M.; Lacour, D.; Andrieu, S.; Chshiev, M.; Hauet, T.; Montaigne, F.; Mangin, S.; Han, X. F.; Lu, Y. Long-Range Phase Coherence in Double-Barrier Magnetic Tunnel Junctions with a Large Thick Metallic Quantum Well. *Phys. Rev. Lett.* 2015, *115* (15), No. 157204.

(15) Yuasa, S.; Fukushima, A.; Kubota, H.; Suzuki, Y.; Ando, K. Giant Tunneling Magnetoresistance up to 410% at Room Temperature in Fully Epitaxial Co/MgO/Co Magnetic Tunnel Junctions with Bcc Co(001) Electrodes. *Appl. Phys. Lett.* 2006, *89* (4), No. 042505.

(16) Bonell, F.; Hauet, T.; Andrieu, S.; Bertran, F.; Le Fevre, P.; Calmels, L.; Tejeda, A.; Montaigne, F.; Warot-Fonrose, B.; Belhadji, B.; Nicolaou, A.; Taleb-Ibrahimi, A. Spin-Polarized Electron Tunneling in Bcc FeCo/MgO/FeCo(001) Magnetic Tunnel Junctions. *Phys. Rev. Lett.* 2012, *108* (17), No. 176602.

(17) Andrieu, S.; Calmels, L.; Hauet, T.; Bonell, F.; Le Fevre, P.; Bertran, F. Spectroscopic and Transport Studies of CoxFe1-x/MgO(001)-Based Magnetic Tunnel Junctions. *Phys. Rev. B* 2014, *90* (21), No. 214406.

(18) Zhang, X. G.; Butler, W. H. Large Magnetoresistance in Bcc Co/MgO/Co and FeCo/MgO/FeCo Tunnel Junctions. *Phys. Rev. B* 2004, *70* (17), No. 172407.

(19) Ma, T.; Zhu, Y.; Dainone, P. A.; Chen, T.; Devaux, X.; Wan, C.; Migot, S.; Lengaigne, G.; Vergnat, M.; Yan, Y.; Han, X.; Lu, Y. Large Sign Reversal of Tunneling Magnetoresistance in an Epitaxial Fe/MgAlOx/Fe4N Magnetic Tunnel Junction. *ACS Appl. Electron. Mater.* 685
2023, *5* (11), 5954−5961.

(20) Yang, B.; Tao, L.; Jiang, L.; Chen, W.; Tang, P.; Yan, Y.; Han, X. Ultrahigh Tunneling-Magnetoresistance Ratios in Nitride-Based Perpendicular Magnetic Tunnel Junctions from First Principles. *Phys. Rev. Appl.* 2018, *9* (5), 54019.

(21) Mi, W. B.; Guo, Z. B.; Feng, X. P.; Bai, H. L. Reactively Sputtered Epitaxial Gamma '-Fe4N Films: Surface Morphology, Microstructure, Magnetic and Electrical Transport Properties. *Acta Mater.* 2013, *61* (17), 6387−6395.

(22) Yuasa, S.; Nagahama, T.; Fukushima, A.; Suzuki, Y.; Ando, K. Giant Room-Temperature Magnetoresistance in Single-Crystal Fe/MgO/Fe Magnetic Tunnel Junctions. *Nat. Mater.* 2004, *3* (12), 868− 871.

(23) Duluard, A.; Bellouard, C.; Lu, Y.; Hehn, M.; Lacour, D.; Montaigne, F.; Lengaigne, G.; Andrieu, S.; Bonell, F.; Tiusan, C. Enhanced Magnetoresistance by Monoatomic Roughness in Epitaxial Fe/MgO/Fe Tunnel Junctions. *Phys. Rev. B* 2015, *91* (17), No. 174403.

(24) Lu, Y.; Yang, H.-X.; Tiusan, C.; Hehn, M.; Chshiev, M.; Duluard, A.; Kierren, B.; Lengaigne, G.; Lacour, D.; Bellouard, C.; Montaigne, F. Spin-Orbit Coupling Effect by Minority Interface Resonance States in Single-Crystal Magnetic Tunnel Junctions. *Phys. Rev. B* 2012, *86* (18), No. 184420.

(25) Tao, B. S.; Jiang, L. N.; Kong, W. J.; Chen, W. Z.; Yang, B. S.; Wang, X.; Wan, C. H.; Wei, H. X.; Hehn, M.; Lacour, D.; Lu, Y.; Han, X. F. Tunneling Anisotropic Magnetoresistance in Fully Epitaxial Magnetic Tunnel Junctions with Different Barriers. *Appl. Phys. Lett.* 2018, *112* (24), No. 242404.

(26) Ravensburg, A. L.; Palsson, G. K.; Pohlit, M.; Hjoervarsson, B.; Kapaklis, V. Influence of Misfit Strain on the Physical Properties of Fe Thin Films. *Thin Solid Films* 2022, *761*, No. 139494.

(27) Sukegawa, H.; Xiu, H.; Ohkubo, T.; Furubayashi, T.; Niizeki, T.; Wang, W.; Kasai, S.; Mitani, S.; Inomata, K.; Hono, K. Tunnel Magnetoresistance with Improved Bias Voltage Dependence in Lattice-Matched Fe/Spinel MgAl2O4/Fe(001) Junctions. *Appl. Phys. Lett.* 2010, *96* (21), No. 212505.
(28) Smith, N.; Brookes, N.; Chang, Y.; Johnson, P. Quantum-Well and Tight-Binding Analyses of Spin-Polarized Photoemission from Ag/Fe(001) Overlayers. *Phys. Rev. B* 1994, *49* (1), 332−338.
(29) Potapov, P. Why Principal Component Analysis of STEM Spectrum-Images Results in “Abstract”, Uninterpretable Loadings? *Ultramicroscopy* 2016, *160*, 197−212.
(30) Kresse, G.; Hafner, J. Ab Initio Molecular Dynamics for Liquid Metals. *Phys. Rev. B* 1993, *47* (1), 558−561.
(31) Kresse, G.; Furthmuller, J. Efficiency of Ab-Initio Total Energy Calculations for Metals and Semiconductors Using a Plane-Wave Basis Set. *Comput. Mater. Sci.* 1996, *6* (1), 15−50.
(32) Kresse, G.; Furthmuller, J. Efficient Iterative Schemes for Ab Initio Total-Energy Calculations Using a Plane-Wave Basis Set. *Phys. Rev. B* 1996, *54* (16), 11169−11186.